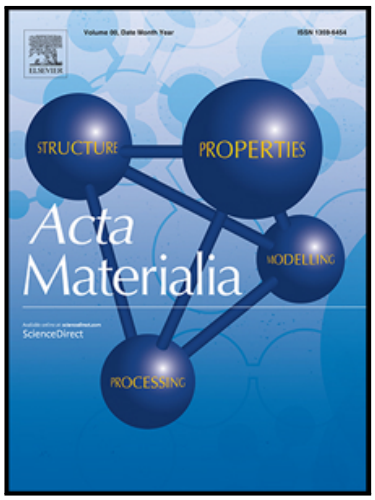

In situ synchrotron investigation of degenerate graphite nodule evolution in ductile cast iron

T. Wigger , T. Andriollo , C. Xu , S.J. Clark , Z. Gong ,
R.C. Atwood , J.H. Hattel , N.S. Tiedje , P.D. Lee , M.A. Azeem

PII: S1359-6454(21)00746-1
DOI: https://doi.org/10.1016/j.actamat.2021.117367
Reference: AM 117367

To appear in: *Acta Materialia*

Received date: 15 March 2021
Revised date: 15 September 2021
Accepted date: 30 September 2021

Please cite this article as: T. Wigger , T. Andriollo , C. Xu , S.J. Clark , Z. Gong , R.C. Atwood , J.H. Hattel , N.S. Tiedje , P.D. Lee , M.A. Azeem , In situ synchrotron investigation of degenerate graphite nodule evolution in ductile cast iron, *Acta Materialia* (2021), doi: https://doi.org/10.1016/j.actamat.2021.117367

In situ synchrotron investigation of degenerate graphite nodule evolution in ductile cast iron

T. Wiggera,b,*, T. Andriolloc, C. Xuc, S. J. Clarka,d, Z. Gonga,b, R. C. Atwoode, J. H. Hattelc, N. S. Tiedjec, P. D. Leea,b,*, M. A. Azeemb,f,*

*Corresponding authors.

t.wigger@ucl.ac.uk +44 1235567823, peter.lee@ucl.ac.uk +44 1235567789, mohammed.azeem@leicester.ac.uk +44 1162297422

[a] University College London, Mechanical Engineering, London WC1E 7JE, UK
[b] Research Complex at Harwell, Harwell Campus, Didcot OX11 0FA, UK
[c] Technical University of Denmark, 2800 Kgs. Lyngby, Denmark
[d] Argonne National Laboratories, Lemont, IL 60439, USA
[e] Diamond Light Source Ltd, Harwell Campus, Didcot OX11 0DE, UK
[f] University of Leicester, Leicester LE1 7RH, UK

Keywords: Ductile Cast Iron, degenerate graphite morphology, X-ray computed tomography, Growth kinetics

Graphic abstract

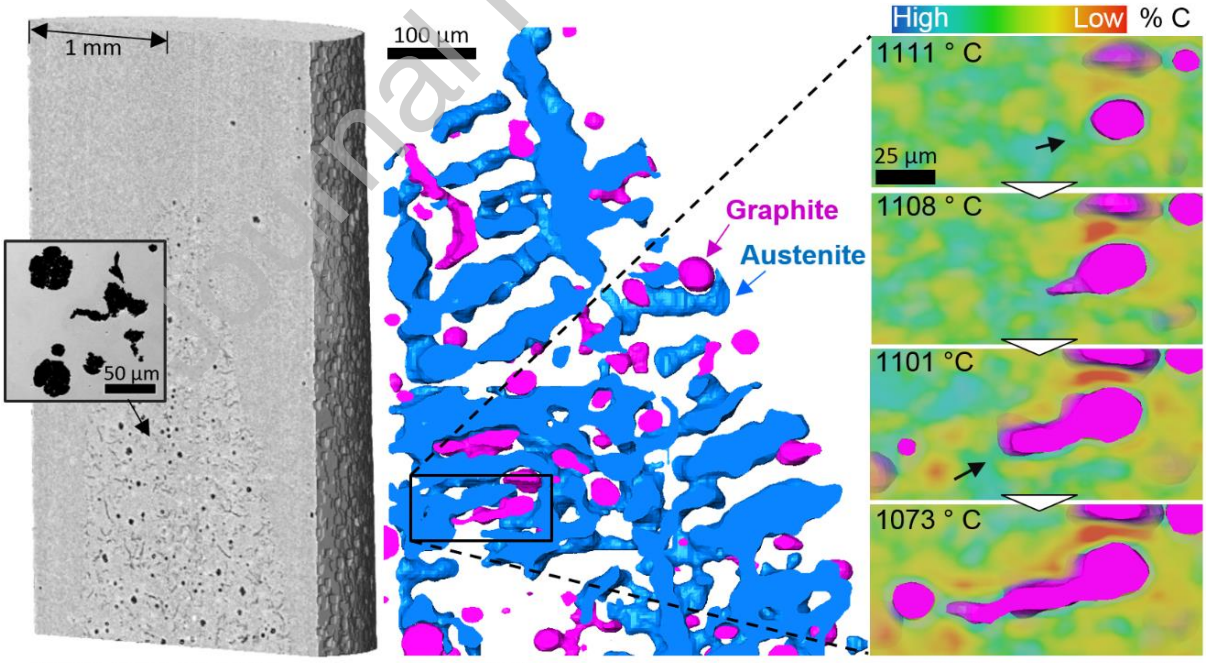

Tomogram showing graphite morphologies in ductile cast iron after six re-melting cycles

Graphite features embedded in austenite dendrites

Formation of degenerate nodule and evolution of carbon concentration field during solidification

Abstract

Ductile cast irons (DCIs) are of increasing importance in the renewable energy and transportation sectors. The distribution and morphology of the graphite nodules, in particular the formation of degenerate features during solidification, dictate the mechanical performance of DCIs. *In situ* high-speed synchrotron X-ray tomography was used to capture the evolution of graphite nodules during solidification of DCI, including degenerate features and the effect of the carbon concentration field. The degeneration of nodules is observed to increase with re-melting cycles, which is attributed to Mg-loss. The dendritic primary austenite and carbon concentration gradients in the surrounding liquid phase were found to control nodule morphology by locally restricting and promoting growth.

A coupled diffusion-mechanical model was developed, confirming the experimentally informed hypothesis that protrusions form through liquation cracking of the austenite shell and subsequent localised growth. These results provide valuable insights into the solidification kinetics of cast irons, supporting the design of advanced alloys.

1. Introduction

Ductile Cast Iron (DCI), or nodular cast iron, is critical for various industrial sectors, such as transportation and renewable energy production. DCIs are easily castable, whilst offering excellent mechanical properties at a low production cost per unit weight [1]. The unique ability of DCIs to dampen loads combined with relatively high ductility and toughness in comparison with other cast irons [2], makes them ideal candidates for cyclic loading applications, such as in wind turbines [3] and large marine propulsion systems [4]. These

and other applications of DCIs, amount to more than a fifth of the worldwide casting production by weight [5]; therefore, significant improvements of the production process will have a large impact across various industrial sectors.

DCIs have a unique microstructure consisting of graphite nodules embedded in a multi-phase metallic matrix, essentially forming a metal matrix composite. The shape and size of these graphite nodules dictate the mechanical properties of DCIs, such as fatigue resistance [6,7] and strength [8]. Various forms of degenerate, i.e. non-spherical graphite nodules, have been observed in DCIs [9–11], forming alongside spherical and sometimes star-shaped nodules during solidification. In advanced commercial DCI production, both post solidification microstructural observations and modelling are used to identify solidification pathways in order to suppress the formation of degenerate, i.e. aspherical nodules. Until recently, the nucleation, growth kinetics and morphology of nodules during solidification were studied *ex situ* by interrupted quenching experiments, which are often time consuming and highly resource intensive [12,13]. Confocal microscopy was utilised to characterise nodules [14] and δ - γ transformations [15]. Although, by investigating a large sample area, it is feasible to gather a representative microstructural information about nucleation and growth by post-solidification characterisation, it is impossible to capture the time dependent nucleation, growth and degeneration of individual nodules. Thus, in order to obtain real-time microstructural information, advanced characterisation techniques such as X-ray radiography and tomography are crucial.

Synchrotron X-ray light sources have evolved dramatically over the last two decades. With the incorporation of fast acquisition systems it is now possible to capture a vast amount of rich dynamic microstructural information to unravel various underlying mechanisms [16–

18]. For metallic systems, the first radiographic imaging dataset of dendritic microstructures during solidification was obtained on a Al-30 wt% Cu alloy [19]. Several radiographic studies have been conducted since, on low melting point alloys and a wide range of microstructural aspects, for instance formation of secondary phases [20] and defects such as porosity [21,22].

However, even with such large strides in radiographic imaging of low melting alloys, there were only a select few studies on high melting point alloys, such as Fe [17,23]. These observations on Fe-C alloys provided first insights into the formation and growth of Fe dendrites during solidification. Dendrite fragmentation in Fe-C alloys was reported [24] as a result of grain boundary melting post δ-γ phase transformation during interrupted solidification, in the presence of carbon rich liquid in vicinity. In a recent investigation, the nucleation and growth of predominantly regular nodules was observed in a DCI alloy along with gamma dendrites during continuous cooling [17]. Whilst radiographic imaging is fast, the constraining sample geometry has a major impact on the microstructure evolution in the liquid-solid regime during solidification. These geometric constraints are almost absent in relatively larger samples that are used in tomographic imaging.

In situ 3D tomography has been used for solidification investigations in low melting point alloys for more than a decade [25–31]. The development of advanced high temperature environmental cells and high X-ray contrast alloy systems now provides a toolset to investigate dendritic patterns in Co, Ni and Fe [29]. Tomography has also been used for capturing solid state defect features in Al alloys [32], Ti alloys [33] and for damage quantification during deformation in the semi-solid regime [27,34]. Recently, the first tomographic investigation to capture nucleation and growth of regular and degenerate

nodules in a DCI alloy was published [35]. The graphite evolution and growth of protrusions (or polyps) from initially spherical nodules was captured, and it was hypothesised that these protrusions form as a result of liquation cracking [35,36]. However, due to restricted X-ray flux, the temporal resolution was low, requiring 40 s to capture each tomogram. The interplay of graphite with the surrounding solid austenitic structures and carbon concentrations during solidification, and how exactly those affect the graphite morphology and growth directions, remained unclear. Further, it is yet to be explored if there are transition states between spherical, degenerate and vermicular graphite shapes.

To build robust global microstructure prediction tools, it is necessary to understand normal and abnormal growth of graphite nodules in DCIs. It is equally important to understand the effect of thermal fluctuations on the local microstructure. Several numerical models have been proposed to describe nodule growth ranging from a 1D spherical coordinate model [37] (based on a uni-nodular approach [38]) to a 3D Phase Field simulation [39]. These models assume uniform spherical nodule growth, degenerate morphologies are not taken into consideration. The primary computational objective of this study is to provide a modelling framework for predicting the growth of degenerate features during solidification of DCIs.

In this investigation, the regular growth of nodules is captured with a temporal resolution ten times faster than our previous experiment [35]. The high flux and faster acquisition allowed for accurately capturing the changes in the carbon concentration field in the melt, *via* the variation in attenuation. The effects of the change in chemical composition (in particular the loss of Mg) during long cooling times in large industrial scale castings is emulated by thermal cycling with remelting and solidification between 1180 °C and 1000 °C.

This also permitted the observation of the effect of Mg loss on the sphericity of nodules during prolonged heating. As the formation of degenerate features during each cooling cycle are captured at unprecedented temporal and spatial resolution, the results provide vital insights into the evolution of the full range of graphite nodule morphologies, revealing the role of the solid phase and the surrounding carbon concentration field in the formation of degenerate features. A 2D numerical model is developed, based on carbon diffusion and mechanical forces imposed on the austenite shell by the encapsulated nodule, allowing predictions of variations in graphite growth and morphology. The results presented are critical for understanding the physical processes occurring during the productions of DCIs, thus enabling the design of new alloys and targeted optimisation of industrial casting pathways of existing alloys.

2. Methods

2.1 *In situ* Synchrotron X-ray tomography and sample environment

The experiment was performed at the I12-JEEP beamline of Diamond Light Source, UK [40]. The beamline provides high energy and photon flux for high-speed tomography. A ductile cast iron alloy was used in the experiments, containing 1.94 ± 0.02 wt.% Si for stabilisation of the graphite and 0.075 ± 0.005 wt.% Mg to enable the formation of graphite nodules. The overall composition is given in Table 1. The alloy used had the same composition and properties as in our previous publication [35]. The specimen was manufactured by melting the alloy in an induction furnace and casting it into a 500g ingot, from which a cylindrical sample with Ø2 mm diameter and 12 mm height was prepared by electric discharge machining (EDM). The sample was encapsulated in an argon filled quartz glass tube with 2.1

mm internal diameter to prevent reactions with the environment and held in place by a tight-fitting quartz rod at the bottom of the capsule [35] (Fig. 1 (a)).

Table 1: Composition, liquidus, equilibrium eutectic and solidus temperatures of the ductile cast iron alloy used in the experiment. The standard deviations are based on 5 measurements and given in parentheses.

Element	C	Si	Mn	Mg	P	S	Fe
Concentration (wt.%) (STDV)	3.43 (0.02)	1.94 (0.02)	0.11 (0.002)	0.07 (0.005)	0.014 (0.005)	0.006 (0.005)	balance
Liquidus temperature	1180 °C						
Eq. eutectic temperature	1162 °C						
Solidus temperature	1090 °C						

The encapsulated specimen was fixed to an alumina sample module (Fig. 1 (b)) which was mounted on the beamline rotation stage. The entire assembly was carefully placed concentrically in the bespoke high-temperature Alice environmental cell [29] (Fig. 1 (a)). Temperatures were measured with an R-type thermocouple placed at about 1 mm distance from the quartz encapsulated sample (Fig. 1 (c)). Specimen and furnace were then aligned with the X-Ray beam and the PCO.edge camera used for acquisition. Monochromatic X-rays with an energy of 61 keV (0.2 Å wavelength) were used, and each projection was captured with a resolution of 3.24 μm^2 per pixel in a 1600x1080 $pixel^2$ field of view (FOV). The distance between detector and specimen was 750 mm.

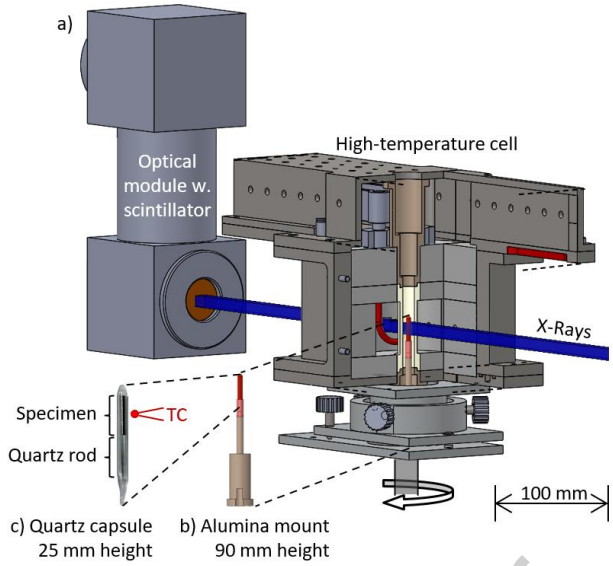

Fig. 1: (a) Schematic of the high temperature Alice environmental cell setup at the I12 beamline of Diamond Light Source with optical module, (b) schematic of the sample module with alumina sample mount and (c) image of the quartz encapsulated sample with the location of the thermocouple (TC).

The specimen was subjected to six (re-)melting cycles (Supplementary Fig. S1). During each cycle, it was heated up to 1180 ± 0.5 °C just above $T_{liquidus}$, held for 30 s to ensure that the specimen was homogeneously molten, and finally cooled down at 0.3 °C/s to 1000 ± 0.5 °C, 90 °C below the solidus. A sequence of 150 tomograms was continuously recorded during each cooling ramp, with 720 projections over 180° per tomogram. The exposure time for every projection was 5 ms and the frame rate 182 Hz, resulting in 4 s acquisition time per tomogram. The acquired FOV captured microstructural changes in the top 4 mm of the 8 mm specimen.

The images were reconstructed using Savu [41,42], obtaining tomograms of 920 x 930 x 1060 voxels^3 and Avizo 2019.1 (Thermo Fisher Scientific Inc.) was utilised for image

processing and visualisation (Supplementary Fig. S2). For the quantification of the graphite phase, the minimum size for a segmented particle to be counted as a nodule was 27 voxels.

2.2 Model

A single, spherical nodule of radius 10 µm is considered as fully encapsulated in a 15 µm thick austenite shell. The shell is in contact with the liquid on the outside and contains a notch that reduces its thickness locally to 3 microns. The shape of the notch is such that the entire system can be considered axisymmetric with respect to the horizontal axis shown as dashed line in Fig. 2. The presence of the notch breaks the spherical symmetry of the system, allowing simulation of the effect of the inhomogeneous diffusion of carbon atoms through the shell on the local growth rate of the nodule.

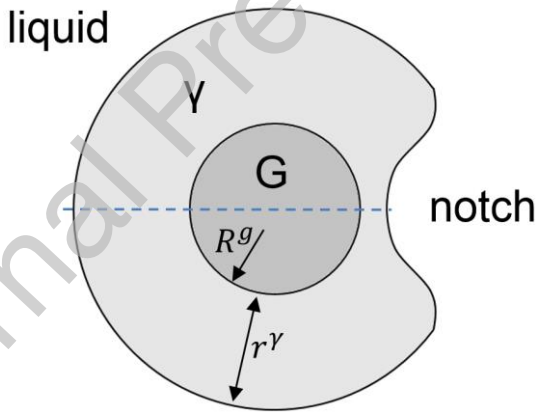

Fig. 2: Illustration of the 2D diffusion-mechanical model. The geometry is rotation-symmetric (axis indicated with blue dashed line). The graphite nodule G has radius R^g and the austenite shell thickness is r^γ, except for the thinner notch with 1/5 r^γ.

Under the assumption that the austenite grows slowly and uniformly in all directions, we are considering this growth as negligible and the mass of the austenite as constant during the considered time interval. The austenite shell is modelled as a deformable material

according to the standard Lagrangian framework of continuum mechanics [43]. The region occupied by the austenite γ is defined as Ω and the interfaces with the liquid and with the graphite are indicated by $\partial\Omega^L$ and $\partial\Omega^g$, respectively. The mechanical deformation of the shell is driven by the growth of the nodule, which occurs due to carbon diffusion from the liquid through the shell. In order to describe this phenomenon, the well-known diffusion equation is solved on Ω:

$$\frac{\partial w_C^\gamma}{\partial t} = \mathrm{div}\left(D_c^\gamma \cdot \nabla w_C^\gamma\right) \tag{1}$$

where w_C^γ denotes the Carbon mass fraction, t is the time variable, D_c^γ is the Carbon diffusion coefficient and $\mathrm{div}(\cdot)$ and $\nabla(\cdot)$ are the divergence and gradient operators, respectively. Boundary conditions for Eq. (1) are provided by prescribing the value of w_C^γ on $\partial\Omega^L$ and on $\partial\Omega^g$ according to the functions $w_C^{\gamma/L}(T)$ and $w_C^{\gamma/g}(T)$, which are assumed to depend on the temperature T according to the phase diagram. The steady-state solution at time t = 0 s is used as initial condition. In addition to diffusion, the linear momentum balance equation is solved on Ω:

$$\mathrm{div}(\boldsymbol{\sigma}) = \rho\dot{\boldsymbol{v}} \tag{2}$$

where $\boldsymbol{\sigma}$ is the Cauchy stress tensor, ρ is the density, $\boldsymbol{v}$ is the velocity and $\dot{(\cdot)}$ denotes the material time derivative. The velocity field is assumed to be zero at t = 0 s and the value of ρ is adjusted in order to minimise dynamic effects on the solution. The boundary conditions for Eq. (2) are as follows. Zero surface traction is imposed on $\partial\Omega^L$ by neglecting the pressure of the liquid. Conversely, the value of $\boldsymbol{v}$ is prescribed on $\partial\Omega^g$ based on the assumption that the local velocity of the graphite-austenite interface depends solely on the flux density of carbon atoms $\boldsymbol{\phi}_C$ according to the expression:

$$\boldsymbol{v} \cdot \boldsymbol{n} = -\frac{1}{\rho^g} \boldsymbol{\phi}_C \cdot \boldsymbol{n} \tag{3}$$

where ρ^g and $\boldsymbol{n}$ denote the graphite density and interface unit normal, respectively. By means of Fick's first law, Eq. (3) can be re-written as:

$$\boldsymbol{v} \cdot \boldsymbol{n} = \mu D_c^\gamma \nabla w_C^\gamma \cdot \boldsymbol{n} \tag{4}$$

with μ indicating the ratio between the densities of the austenite and of the graphite. It is worth noting that Eq. (4) expresses the effect of diffusion on the mechanical deformation of the austenite shell in the model. In turn, the shell deformation affects the diffusion by progressively changing the geometry of the domain Ω. Concerning the mechanical behavior of the austenite, an isotropic linear elastic-perfectly plastic response is assumed, with the flow behaviour described by the standard J2 (von Mises) plasticity theory. This assumption is simplistic, given the very complex behaviour of the austenite close to the melting point. However, since the model mechanical deformation is controlled by Eq. (4), the choice of the constitutive model and of its parameters is not expected to alter the computed velocity field radically, which is the quantity of interest in the present case. This has been verified by varying the value of the yield stress in the present model over several orders of magnitude.

We have selected the following parameters for the model:

$$D_c^\gamma = 100\ \mu m^2/s,\ \mu = 4,\ w_C^{\gamma/L} = 2\%,\ w_C^{\gamma/g} = 1.8\%,$$

$$E^\gamma = 10\ GPa,\ \nu^\gamma = 0.3,\ \sigma_y^\gamma = 0.1\ MPa$$

where E^γ, ν^γ and σ_y^γ are the Young's modulus, Poisson's ratio and yield stress of the austenite.

The entire model was implemented in the finite element software Abaqus/Explicit, due to its capability to handle non-linear, fully coupled diffusion-mechanical analyses in a Lagrangian framework. The model implementation was straightforward except for the enforcement of the non-standard boundary condition (4), which required the development of an ad hoc procedure, presented in Supplementary Note 3.

3. Results and discussion

Sections of the tomograms obtained after the first, third and the sixth solidification cycle are shown in Fig. 3 a, b and c respectively. Continuous change during the solidification stage of each cycle is shown in Supplementary videos V4a, V4b and V4c. The greyscale in Fig. 3 is proportional to the atomic number, as X-ray attenuation increases with higher Z elements, with the graphite phase (carbon) dark and the iron rich surrounding liquid and metallic phases bright. The evolution of these phases melting and solidifying is captured during the repeated thermal cycling between liquidus and solidus of the DCI.

After the first cycle (Fig. 3 (a)), a large number of regular spherical nodules of various size appear, homogeneously distributed across the entire specimen. In subsequent cycles, the number of regular nodules decreases, such that the specimen is clearly divided into three distinct regions; **R1** which is predominantly composed of regular graphite nodules and some vermicular (compacted) graphite, **R2** is composed of predominantly vermicular and a few nodular graphite particles and **R3** is the outermost region comprised of fine lamellar graphite, as in grey cast iron. These three regions are marked in Fig. 3(c). Morphologically, there is a clear demarcation between regions R2 and R3, contrary to R1 and R2. The lamellar

graphite in R3 is so fine that individual lamellae remain unresolved in the current imaging conditions. However, the existence of these flakes changes the X-ray attenuation, causing the contrast difference.

The morphology transition of graphite from nodular to vermicular and subsequently to lamellar is due to progressive loss of Mg to the ambience [9] with each re-melting cycle. The loss of Mg is higher in the outer regions of the sample compared to the centre and possibly exacerbated to some degree due to flotation of nodules during early cycles, hence causing the bell shape. In the context of large castings, this is a very important factor, as any flotation alters the Mg content and hence changes the nodule morphology from bottom to top.

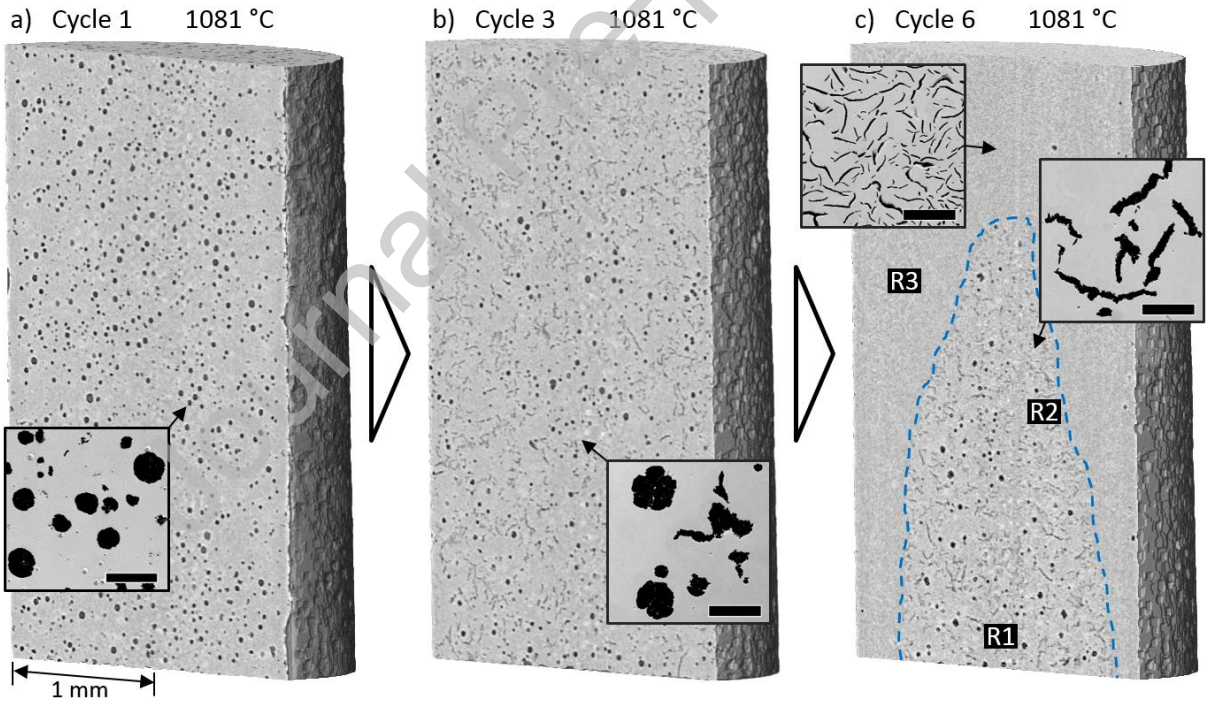

Fig. 3: Centre sections of the tomograms recorded at 1081 °C after (a) the first thermal cycle, (b) the third and (c) the sixth thermal cycle. Only nodular graphite develops during the first cycle (a), whilst various other forms of graphite develop during the subsequent

cycles. Grey Iron (R3) forms at the top and sides of the specimen and a mixture of nodular and vermicular graphite forms in the centre and at the bottom. The insets are optical micrographs obtained by microscopy on specimen sections post solidification, with scale bars of 50 µm length. The continuous transition of each cycle is shown in Supplementary videos V4a, V4b and V4c.

During both the first and last cycle, the first austenite dendrites appear around 1160 °C (Supplementary video V4a, V4c), although partly obscured by the high noise level. In cycle 1, the first nodules are observed at around 1135 °C, some of which remain in place between the dendrites, others float upwards and get trapped in the evolving dendrite network closer to the top. The blurred or streaky appearance of some nodules is a consequence of their ascent during the 4 second tomogram acquisition time, resulting in artefacts generated during reconstruction. In a recent *in situ* radiography investigation [17], nodule flotation is observed to occur over varying distances. The nodule nucleation then progresses in form of a wave from bottom to top.

In cycle 6, the dendrites are engulfed by grey iron around 1135 °C, this is seen to happen from bottom to top (refer Supplementary video V4c), forming an enclosed semi-solid space which tapers from bottom to top in the central region of the specimen. Below 1130 °C, nodules and vermicular graphite nucleate simultaneously in the remaining liquid. In all six cycles, there are very few microstructural changes observed below 1090 °C. The temperature range in which nodular and vermicular graphite formed in the current investigation matches well with our previous observation on regular and irregular nodules (supplementary information to [35]).

3.1 Global sphericity evolution

As a consequence of the Mg loss and the changes in phase composition, the number of nodules is observed to reduce dramatically with thermal cycling, as evident in Fig. 4. From cycle 1 to 6, the number of nodules per mm^3 (N_v) is reduced by about one order of magnitude, from 3560 ($N_{v,t,C1}$) to 370 ($N_{v,t,C6}$). Furthermore, a significantly different sphericity distribution is evident: After cycle 1, most nodules have a sphericity of 0.7 or higher ($N_{v,t>0.7,C1}$ = 3460 or 97% of $N_{v,t,C1}$). After cycle 6, the $N_{v,t>0.7,C6}$ is 320, which is 86% of $N_{v,t,C6}$. Repeated re-melting and Mg-loss thus reduces the total number of nodules and as well as the sphericity.

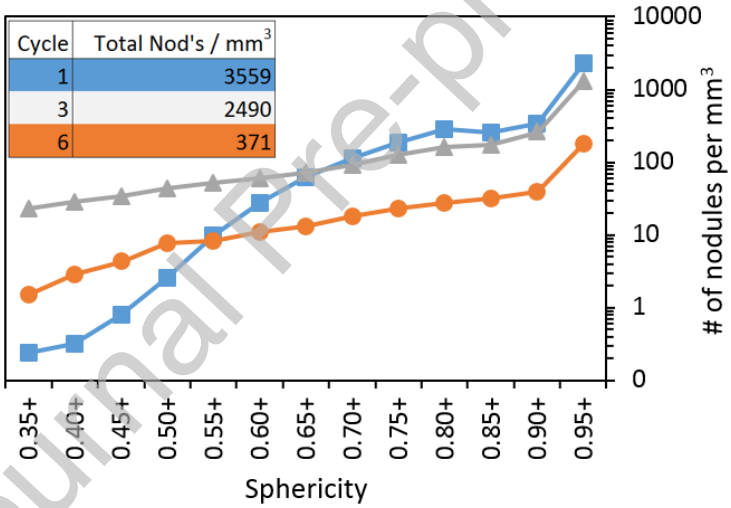

Fig. 4: Distribution of nodules per mm^3 as a function of sphericity, after cycle 1 (blue), cycle 3 (grey) and cycle 6 (orange).

3.2 Formation of degenerate features

Degenerate features increase the tendency of DCI to crack during loading, especially in the case of cyclic loading where cracks may initiate from the sharp edges of thin protrusions. In

order to gain deeper understanding of the sequence in which degenerate features are formed, representative sub-volumes are selected and the development of the feature morphology is tracked, as shown in Fig. 5 for the case of cycle 3. Due to loss of Mg in the first 2 cycles, a higher number of degenerate features has formed, and their evolution is investigated in relation to the surrounding phases. Sections of a graphite nodule developing a protrusion over several time and temperature steps are presented as 2D slices extracted from tomograms, Fig. 5 (a-f). The corresponding 3D segmented volumes of the region are shown in (g-l), with the graphite nodules in magenta. The black dashed line in Fig. 5 (g) indicates the section plane of the 2D images perpendicular to the 3D view. The data provided in Fig. 5 is a short sub-set of a larger sequence of tomograms, the full data from this selected region is provided in Supplementary Video V5.

As the X-Ray attenuation of any material generally increases with its density, graphite with its low density appears darker than the surrounding liquid and metallic phases in the left column of Fig. 5. A dark nodule nucleates at 1115 °C in the top right of (Fig. 5 (a)) within a slightly noisy field and grows to a sphere of ~20 µm in Fig. 5 (b). A large protrusion forms sideways from the nodule in a range from 1108 °C to 1101 °C (Fig. 5 (c – e)), which then in turn produces another sub-protrusion during further cooling, as evident in the solid state at 1073 °C (Fig. 5 (f)).

Assuming that the higher carbon concentration in the liquid and solid surroundings also reduces their density and hence their X-Ray attenuation, the carbon concentration around the nodule is mapped qualitatively in the right column of Fig. 5. High intensities are distributed irregularly in the matrix, excluding fringe and refraction artefacts in the tomograms as a cause, as these would appear near-uniformly around all nodules. High

amounts of C indicate melt and are coloured in blue, low amounts represent austenite and are marked as yellow/red, with the nodule in purple for sufficient contrast. After nucleating at about 1115 °C in an inhomogeneous C-concentration field (Fig. 5(g)), the nodule grows to a nearly spherical shape during cooling to 1111 °C (Fig. 5 (h)). A shell-shaped region of austenite forms around the nodule, however with a liquid-filled opening (black arrow). In the next step at 1108 °C (Fig. 5 (i)), the graphite is protruding from the nodule through the opening, further filling the liquid region next to the nodule at 1107 °C (Fig. 5 (j)). Upon further growth, a new channel opens in the austenite shell in front of the protrusion at 1101 °C (Fig. 5 (k)) with the graphite forming a sub-protrusion through this channel. Such cascading bead-shapes are probably the result of protrusions growing to similar sizes as their parent nodule, as hypothesised in [35].The approximate growth rates of both protrusions are given in Table 2.

Table 2: Approximate growth rates of protrusions from graphite nodule in Fig. 5

Primary protrusion	1.3 µm/s
Secondary protrusion	1.7 µm/s

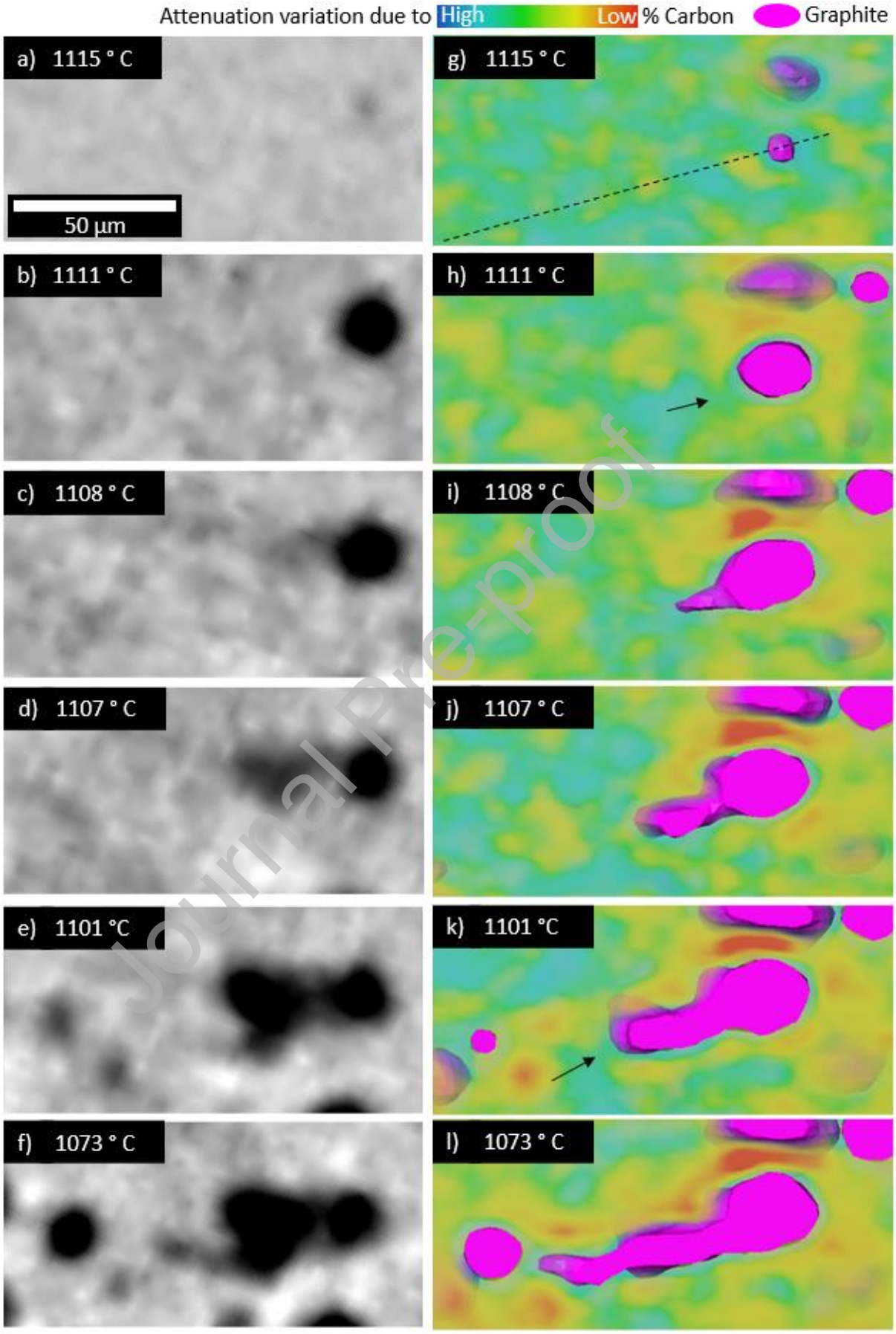

Fig. 5: Evolution of a graphite protrusion from a spherical nodule in the semi-solid matrix during the third re-melting cycle, as tomogram slices on the left (a-f) and segmented 3D on the right (g-l). The black dashed line in (g) shows the section plane perpendicular to the 3D view for the interpolation-smoothened 2D slices. A graphite nodule nucleates (a, g) and grows to a spherical shape (b, h), whilst developing an austenite shell with a high-carbon channel (arrow), formed after the shell is breached. Upon further cooling, the graphite protrudes through this cannel (c, i), growing (d, j), and developing a new shell with a channel (e, k). Subsequently, a second protrusion grows through this channel (f, l). An animation of the process in 3D is provided in Supplementary Video V5.

It is evident that the austenite shell of the particle in Fig. 5 (g – h) is not homogeneous and fully closed, but of varying thickness with gaps as observed previously in [12].

Due to the limited imaging resolution, we cannot observe directly if the liquid channels are open and in contact with the graphite, or blocked by a thin austenite layer. However, if these channels were open, the preferential growth would simply follow the channel geometry very early on due to immediate access to the Carbon in the melt. It is obvious that the graphite grows in spherical form first (liquid and graphite are divorced) up to tens of micrometres in many cases, before developing protrusions later on. This is further supported by the way in which double protrusions are observed, which develop in an intermittent fashion. A first protrusion grows followed by development of another near-spherical graphite feature. The development of the second protrusion also does not occur immediately, but after a time gap long enough to acquire several tomograms. This indicates that a thin retaining austenite wall develops, blocking the channel and thus arresting the

develop of the first protrusion event (again divorced growth). The second protrusion develops when this wall is breached again.

Thus, we hypothesise that the austenite shell is continuous with varying thickness, where very thin sections seem to give the appearance of open channels in shell due to the limited spatial resolution.

When protrusions develop through these gaps, the growth of graphite generally follows the highest carbon concentration in the field [44]. The C-rich melt regions promote protrusion growth instead of nucleating other nodules, possibly due to lack of supersaturation required for nucleation. Several other nodules form in the same neighbourhood, remaining disconnected during the solidification process. The austenite regions between nodules have the lowest C concentrations, such as in the red area near the top right in Fig. 5 (i) to (l).

3.3 Dendritic morphology of the austenite phase

Dendritic growth in cast irons is closely associated with nucleation and growth of the graphite phase. During solidification of DCIs, the interdendritic spaces and valleys in the secondary arms provide appropriate conditions for nodule nucleation. It is evident that the bead-like growth in the nodule can be correlated with the austenite dendrite morphology. As shown in the discussion above and Fig. 5, the subsequent protrusions leading to degeneration of the nodule spread out along a specific plane and direction. During this growth, the original nodule almost ceases radial growth, except for this specific direction/plane, as evident during cooling below 1108 °C, Figure 5 (i-l). This is caused by depletion of carbon in its shell, and also due to physical restrictions imposed by the

surrounding dendritic austenite. To reveal this effect on the graphite morphology, a section (Fig. 6) of the solid austenite phase around the investigated nodule was segmented and examined. Although the X-Ray attenuation difference and hence the signal-to-noise ratio between solid and liquid was very low, it was possible to extract the approximate dendrite morphology around the nodule. The apparent gap between the austenite and graphite phases in Fig. 6 is a result of the segmentation thresholding settings, with a slightly reduced austenite volume to visibly expose the dendritic structure (supplementary Fig. S6). Clearly, the nodule is situated between the secondary arms of two intertwined dendrites (Fig. 6 (a)).

The left dendrite's primary arm has an angle of about 5° from the vertical axis, the right dendrite about 20°. The growth of the nodule examined in Fig. 5 (marked with a black arrow in Fig. 6 (b)) and other nodules in the same neighbourhood is restricted in approximately vertical direction between the arms of both dendrites (Fig. 6 (b)). Not every nodule in the neighbourhood evolves and assumes a degenerate shape, indicating that the formation of degenerate feature is a more local phenomenon, dictated by the surrounding austenite dendrites and carbon concentration. It indicates that on a larger scale, the growth direction of degenerate structures follows the orientation of the austenite dendrites and their interdimeric spaces or spaces between secondary arms. This confirms our hypothesis that protrusions spread from nodules through channels in the surrounding austenite [35]. As soon as further spherical growth is blocked by the solid, the graphite growth occurs sideways. Preferred dendrite orientations may thus have effects on the graphite orientation and may cause some degree of anisotropy in material properties, if the austenite dendritic grains are preferentially oriented due to strong thermal gradients.

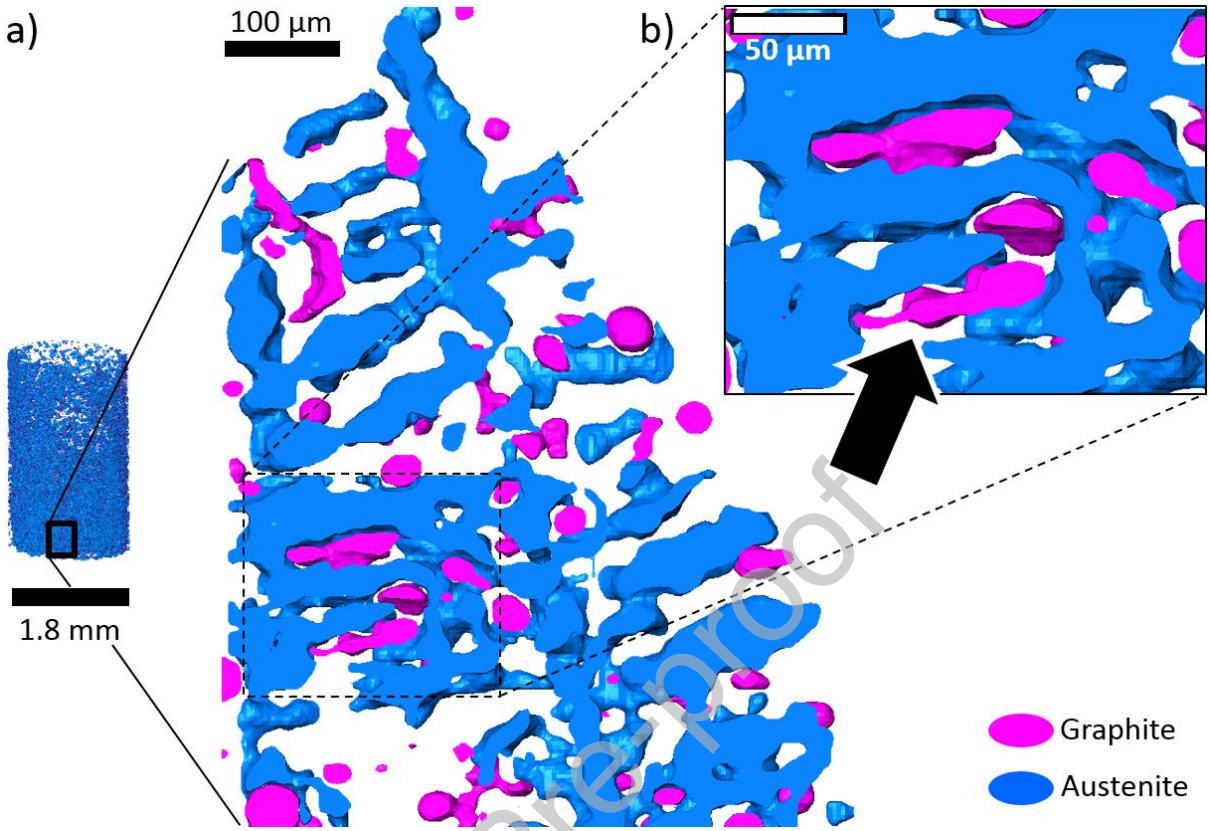

Fig. 6: (a) Segmented austenite phase (blue) in the region around the investigated nodule (Fig. 5) in cycle 3 at 1116 °C, revealing dendritic structures. (b) The graphite protrusions (pink) fill the space between the secondary arms of two entangled dendrites.

3.4 Protrusions from star-shaped nodules

Another nodule morphology observed are so-called “star-shaped” nodules. These form predominantly during later re-melting cycles (no. 4 onwards). Here, an example from cycle 6 is chosen. Unlike regular spherical nodules, these star-shaped nodules do not nucleate in place, but are observed to float up into the FOV from the bottom of the specimen below the scanned region, in a temperature range from 1136 °C to 1120 °C.

These nodules nucleate earlier during solidification in the lower part of the sample (outside the FOV) and float up. We hypothesise that the loss of Mg and carbon from the melt has resulted in a change in the melt chemistry, such that the formation of nodules is facilitated at lower undercooling. The nucleated nodules rise up in the early cooling stages of the later thermal cycles, unrestricted by the austenite matrix. They grow to a critical size [45], permitting radial growth of a few conical sub-crystallites and resulting in a ‘flower-ball’ or ’star’ pattern. Eventually, the floating nodules are caught by the growing dendrites (as seen in Supplemetary Video V4). This mechanism underlines that a change of chemistry combined with local changes in temperature has a profound effect on both graphite nodule morphology and distribution in castings. This may also lead to the so-called “Schwarzbruch”, “Spiking” or “Plate Fracture” which has been observed to occur in the last solidifying regions near feeders in heavy-section ductile iron castings [46–48].

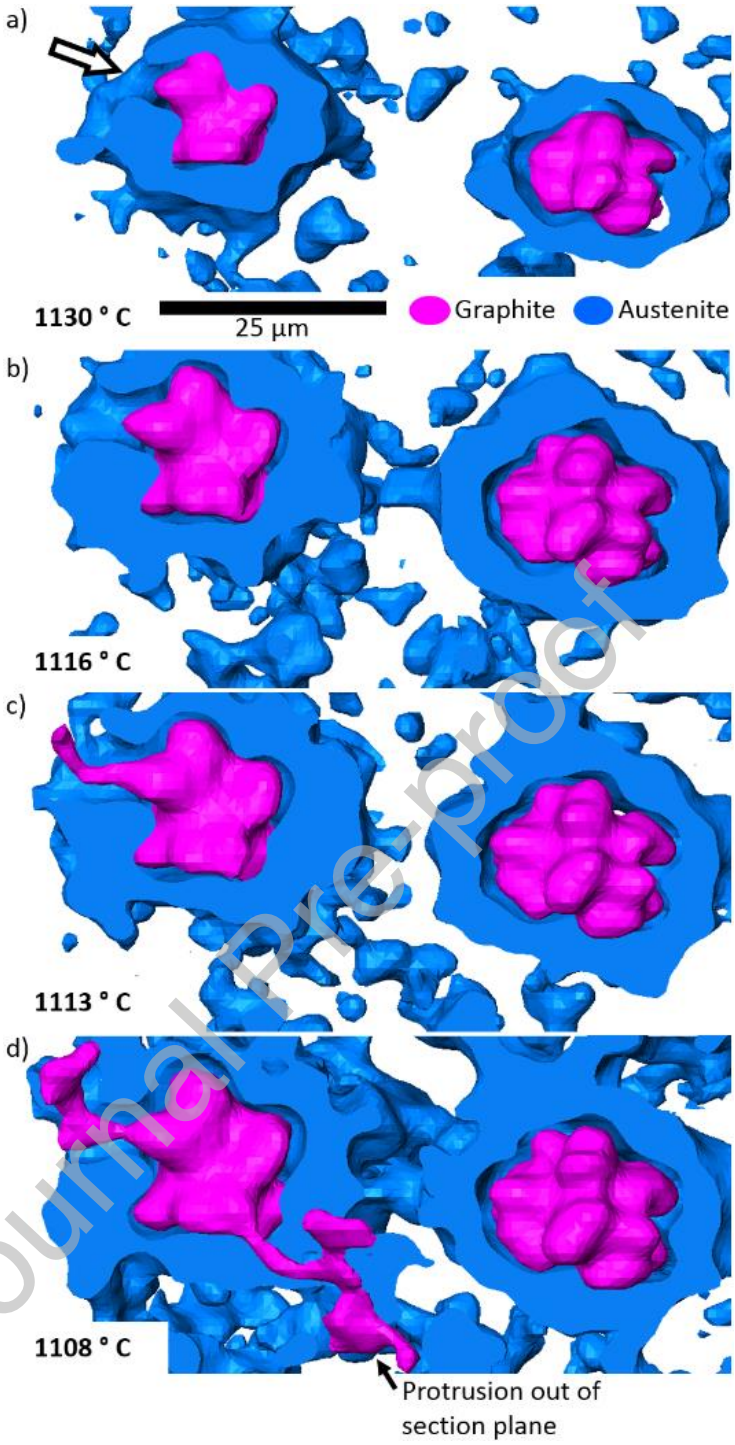

Fig. 7: Evolution of graphite protrusions from star-shaped nodules during cycle 6, developing two protrusions through gaps in the austenite shell on the left (c-d).

Similar to the field around spherical nodules, the carbon concentration around star-shaped nodules is not homogeneous. The apparent gap between austenite and graphite is a result of segmentation settings, as explained above and in supplementary Fig. 6. The austenite shells developed during flotation and the dendritic network they are caught in restrict their growth during subsequent cooling. Fig. 7 shows sections extracted from tomograms captured during the solidification of cycle 6 between 1130 °C and 1108 °C, presenting the evolution of two nodules (pink) and the surrounding low-carbon zone shell (blue). The dendritic microstructure in this vicinity has very low attenuation contrast and could hence not be segmented effectively. The shells around the nodules are seen to have C-rich channels, predominantly in front of the nodule tips, as indicated by the arrow in Fig. 7 (a). The encapsulated nodule and its shell grow during cooling to 1116 °C (b), whilst the C-rich channel remains. A protrusion starts to grow through this channel, emanating from the tip of the nodule at 1113 °C (Fig. 7 (c)). A second protrusion develops from a diametrically opposite tip at 1108 °C, as shown in Fig. 7 (d), although the channel is not visible in the section shown. The morphology of the protrusions, in particular the flat shape of the bottom protrusion, suggests that the graphite spreads by filling gaps between solid structures. The mechanism is similar to spherical nodules, with growth occurring through C-rich channels. The sudden growth of thin features (protrusions) from previously rather uniformly growing features (spheres or stars) suggest that the C-rich channels are originally plugged and then ruptured open by liquation cracking, a similar mechanism to that observed in [27]. The sharp nodule tips or bulged features may lead to stress concentrations in the overlying solid shell.

3.5 Model

A numerical model was developed to test the hypothesis that the growth of graphite nodule protrusions follows the local Carbon concentration. The objective here is to investigate if we can predict the growth direction of the protrusions based on the evolution of the Carbon concentration field. As defined above, the following assumptions are made: The austenite shell is constant in volume and deforms perfectly elastic-plastically. The temporal evolution of the Carbon concentration is dictated by diffusion, where the diffusivity coefficient depends on the Carbon concentration.

Fig. 8 shows the model evolution at two points in time, Fig 8 (a, b) and a representative example of the field around a nodule from the third experimental cycle, Fig 8 (d - f). The model was run with by setting $w_C^{\gamma/L} = 2.0\%$ and $w_C^{\gamma/g} = 1.8\%$. Presuming rotational symmetry around the horizontal axis, this geometry describes a notched sphere in 3D space. The colour coding in the model results shows the deformation velocity of the shell at a point in time, with the arrows indicating the deformation vectors. Other, stress-related quantities are omitted as they heavily depend on the choice of the austenite yield stress, which cannot be determined reliably. Initially (Fig. 8 (a)) the nodule is circular (R = 10 µm) and beginning to expand almost uniformly, with faster expansion in the notched region as indicated in red. The shell expands non-uniformly and predominantly in vertical direction on the outside, due to the asymmetrical load distribution. The deformation vectors of the shell indicate that the notch is widening. After 5 seconds, Fig. 8 (b), the nodule has expanded radially by about 1 µm in the angles with a consistently thick shell, but by up to 3 µm below the notch, forming the foundation of a protrusion. The thinner shell allows faster diffusion at this point,

resulting in locally faster growth of the nodule. On further growth of the protrusion, the shell opens at the notch and the model breaks down – a limitation of this particular design.

In Fig. 8 (d), the nodule is almost perfectly ellipsoidal, but the surrounding high-density shell in yellow has three thin blue channels acting as “notches”. After about 4 seconds (Fig. 8 (e)), three bulges have grown on the nodule at exactly the same positions as the channels. The left and bottom channels are depleted at this point, with the right channel remaining. After another 4 seconds (Fig. 8 (f)), graphite has filled only the left channel, forming a distinct protrusion.

The model confirms our proposition that protrusions develop towards regions with higher carbon gradients in the surrounding field, which cause locally faster diffusion and thus growth, under the condition that the austenite growth is slow compared with the graphite growth. The increasing graphite volume can, according to the model, dilate the shell in these locations to the point of opening (at which the model breaks down), confirming our previous hypothesis of liquation cracking [27,35] as a viable explanation. The carbon will be rejected between the austenite secondary dendrite arms and hence concentrated there, increasing the propensity of protrusions to align with the secondaries, as seen qualitatively in Fig. 6.

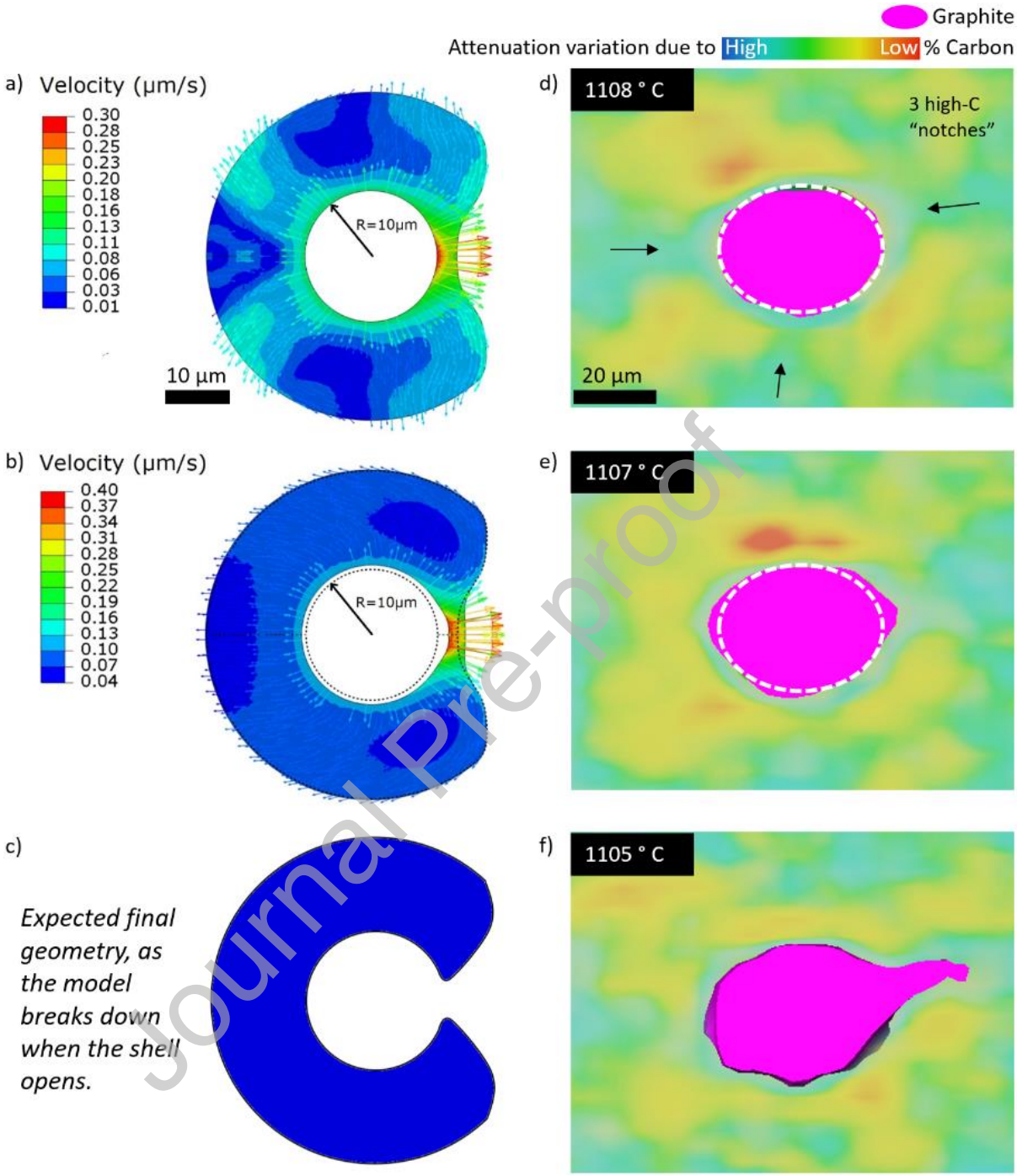

Fig. 8: Comparison of the diffusion-mechanical model (a-c) with experimental results (d-f). The time difference between the model steps is 5 seconds, whilst it is 4 seconds in the experiment. Both model and experiment show accelerated growth towards higher carbon concentrations in vicinity.

4. Conclusions

The development of degenerate graphite morphologies during solidification of nodular cast iron by protrusion growth was investigated using *in situ* synchrotron X-Ray tomography and numerical modelling. The results support the following conclusions:

- Austenite shells around graphite nodules are not homogeneous but they seem to form with varying thickness. The tomography data indicates that there are thinner regions (or open channels) through which carbon can diffuse easily.
- Graphite protrusions form and grow through these higher carbon concentration channels leading to nodule degeneration, which happens in a step-wise fashion with formation of multiple protrusion in certain cases. Their direction and shape is controlled by solid dendrites in the vicinity.
- Large pre-existing nodules can break free and develop star-shapes whilst floating up into hotter regions.
- A 2D axisymmetric finite element model based on carbon diffusion has been implemented, which indicates that the shell with thin sections can deform and open as the nodule grows, thus supporting our experimental observations and theories of liquation cracking in the semi-solid regime during solidification.

Declaration of interests

The authors declare that they have no known competing financial interests or personal relationships that could have appeared to influence the work reported in this paper.

Acknowledgements

This work was made possible by the facilities and support provided by the Research Complex at Harwell and Royal Academy of Engineering (CiET1819/10). This work received support from the Danish Research Council for Independent Research, grant no. 8022-00085B. We are thankful to Diamond Light Source for the awarded beamtime (MG22627) and the assistance of beamline scientists. We also thank Nghia Vo from Diamond Light Source for valuable insights into tomography reconstruction procedures and Jacques Lacaze from CIRIMAT for discussions on phase compositions.

References

[1] D. Stefanescu, ASM Handbook Vol. 1A Cast Iron Science and Technology, ASM International, 2017.

[2] A. Visnapuu, R.W. Nash, P.C. Turner, Damping Properties of Selected Steels and Cast Irons, Bur. Mines Rep. Investig. 9068 (1987).

[3] M.R. Sonne, J.O. Frandsen, J.H. Hattel, Comparison of residual stresses in sand- and chill casting of ductile cast iron wind turbine main shafts, IOP Conf. Ser. Mater. Sci. Eng. 84 (2015). https://doi.org/10.1088/1757-899X/84/1/012025.

[4] E.D. Rejowski, E. Soares, I. Roth, S. Rudolph, Cylinder liner in ductile cast iron for high loaded combustion diesel engines, Proc. ASME 2011 Intern. Combust. Engine Div. Fall Tech. Conf. (2011) 1–8.

[5] Census of World Casting Production, Mod. Cast. (2019) 28–30.

[6] T. Andriollo, Y. Zhang, S. Fæster, V. Kouznetsova, Analysis of the correlation between micro-mechanical fields and fatigue crack propagation path in nodular cast iron, Acta Mater. 188 (2020) 302–314. https://doi.org/10.1016/j.actamat.2020.02.026.

[7] P. Čanžar, Z. Tonković, J. Kodvanj, Microstructure influence on fatigue behaviour of nodular cast iron, Mater. Sci. Eng. A. 556 (2012) 88–99. https://doi.org/10.1016/j.msea.2012.06.062.

[8] L. Collini, G. Nicoletto, Determination of the relationship between microstructure and constitutive behaviour of nodular cast iron with a unit cell model, J. Strain Anal. Eng. Des. 40 (2005) 107–116. https://doi.org/10.1243/030932405X7692.

[9] D.M. Stefanescu, G. Alonso, P. Larrañaga, R. Suarez, On the stable eutectic solidification of iron-carbon-silicon alloys, Acta Mater. 103 (2016) 103–114. https://doi.org/10.1016/j.actamat.2015.09.043.

[10] D.M. Stefanescu, G. Alonso, P. Larrañaga, E. De La Fuente, R. Suarez, On the crystallization of graphite from liquid iron-carbon-silicon melts, Acta Mater. 107 (2016) 102–126. https://doi.org/10.1016/j.actamat.2016.01.047.

[11] H.M. Muhmond, On the Inoculation and Graphite Morphologies of Cast Iron, 2014.

[12] J. Qing, V.L. Richards, D.C. Van Aken, Examination of Spheroidal Graphite Growth and Austenite Solidification in Ductile Iron, Metall. Mater. Trans. A Phys. Metall. Mater. Sci. 47 (2016) 6197–6213. https://doi.org/10.1007/s11661-016-3783-1.

[13] K. Theuwissen, J. Lacaze, L. Laffont, Structure of graphite precipitates in cast iron, Carbon N. Y. 96 (2016) 1120–1128. https://doi.org/10.1016/j.carbon.2015.10.066.

[14] N. Llorca-Isern, J. Tartera, M. Espanol, M. Marsal, G. Bertran, S. Castel, Internal features of graphite in cast irons. Confocal microscopy: Useful tool for graphite growth imaging, Micron. 33 (2002) 357–364. https://doi.org/10.1016/S0968-4328(01)00022-1.

[15] K. Hechu, C. Slater, B. Santillana, S. Clark, S. Sridhar, A novel approach for interpreting the solidification behaviour of peritectic steels by combining CSLM and DSC, Mater. Charact. 133 (2017) 25–32. https://doi.org/10.1016/j.matchar.2017.09.013.

[16] C.L.A. Leung, S. Marussi, R.C. Atwood, M. Towrie, P.J. Withers, P.D. Lee, In situ X-ray imaging of defect and molten pool dynamics in laser additive manufacturing, Nat. Commun. 9 (2018) 1–9. https://doi.org/10.1038/s41467-018-03734-7.

[17] K. Chatcharit, A. Sugiyama, K. Morishita, T. Narumi, K. Kajiwara, H. Yasuda, Time Evolution of Solidification Structure in Ductile Cast Iron with Hypereutectic Compositions, Int. J. Met. 14 (2020) 794–801. https://doi.org/10.1007/s40962-020-00424-3.

[18] M. Rowson, C.J. Bennett, M.A. Azeem, O. Magdysyuk, J. Rouse, R. Lye, J. Davies, S. Bray, P.D. Lee, Observation of microstructure evolution during inertia friction welding using in-situ synchrotron X-ray diffraction, J. Synchrotron Radiat. In Press (n.d.).

[19] E.W.J. Miller, J. Beech, In-situ radiographic observations of alloy solidification, Metallography. 5 (1972) 298–300. https://doi.org/10.1016/0026-0800(72)90009-2.

[20] C. Puncreobutr, P.D. Lee, K.M. Kareh, T. Connolley, J.L. Fife, A.B. Phillion, Influence of Fe-rich intermetallics on solidification defects in Al-Si-Cu alloys, Acta Mater. 68 (2014) 42–51. https://doi.org/10.1016/j.actamat.2014.01.007.

[21] V. Khalajzadeh, D.D. Goettsch, C. Beckermann, Real-time X-ray Radiography and Computational Modeling of Shrinkage Porosity Formation in Aluminum Alloy Castings, Metall. Mater. Trans. A Phys. Metall. Mater. Sci. 50 (2019) 757–771. https://doi.org/10.1007/s11661-018-5018-0.

[22] P.D. Lee, J.D. Hunt, Hydrogen porosity in directional solidified aluminium-copper alloys: In situ observation, Acta Mater. 45 (1997) 4155–4169. https://doi.org/10.1016/S1359-6454(97)00081-5.

[23] H. Yasuda, T. Nagira, M. Yoshiya, N. Nakatsuka, A. Sugiyama, K. Uesugi, K. Umetani, Development of X-ray imaging for observing solidification of carbon steels, ISIJ Int. 51 (2011) 402–408. https://doi.org/10.2355/isijinternational.51.402.

[24] H. Yasuda, K. Morishita, N. Nakatsuka, T. Nishimura, M. Yoshiya, A. Sugiyama, K. Uesugi, A. Takeuchi, Dendrite fragmentation induced by massive-like δ–γ transformation in Fe–C alloys, Nat. Commun. 10 (2019) 1–5. https://doi.org/10.1038/s41467-019-11079-y.

[25] A.B. Phillion, R.W. Hamilton, D. Fuloria, A.C.L. Leung, P. Rockett, T. Connolley, P.D. Lee, In situ X-ray observation of semi-solid deformation and failure in Al-Cu alloys, Acta Mater. 59 (2011) 1436–1444. https://doi.org/10.1016/j.actamat.2010.11.005.

[26] D. Tolnai, P. Townsend, G. Requena, L. Salvo, J. Lendvai, H.P. Degischer, In situ synchrotron tomographic investigation of the solidification of an AlMg4.7Si8 alloy, Acta Mater. 60 (2012) 2568–2577. https://doi.org/10.1016/j.actamat.2012.01.024.

[27] S. Karagadde, P.D. Lee, B. Cai, J.L. Fife, M.A. Azeem, K.M. Kareh, C. Puncreobutr, D. Tsivoulas, T. Connolley, R.C. Atwood, Transgranular liquation cracking of grains in the semi-solid state, Nat. Commun. 6 (2015). https://doi.org/10.1038/ncomms9300.

[28] S. Deville, E. Maire, A. Lasalle, A. Bogner, C. Gauthier, J. Leloup, C. Guizard, In situ X-ray radiography and tomography observations of the solidification of aqueous alumina particle suspensions - Part I: Initial instants, J. Am. Ceram. Soc. 92 (2009) 2489–2496. https://doi.org/10.1111/j.1551-2916.2009.03163.x.

[29] M.A. Azeem, P.D. Lee, A.B. Phillion, S. Karagadde, P. Rockett, R.C. Atwood, L. Courtois, K.M. Rahman, D. Dye, Revealing dendritic pattern formation in Ni, Fe and Co alloys using synchrotron tomography, Acta Mater. 128 (2017) 241–248. https://doi.org/10.1016/j.actamat.2017.02.022.

[30] N. Limodin, L. Salvo, M. Suéry, M. DiMichiel, In situ investigation by X-ray tomography of the overall and local microstructural changes occurring during partial remelting of an Al-15.8 wt.% Cu alloy, Acta Mater. 55 (2007) 3177–3191. https://doi.org/10.1016/j.actamat.2007.01.027.

[31] N. Limodin, L. Salvo, E. Boller, M. Suéry, M. Felberbaum, S. Gailliègue, K. Madi, In situ and real-time 3-D microtomography investigation of dendritic solidification in an Al-10 wt.% Cu alloy, Acta Mater. 57 (2009) 2300–2310. https://doi.org/10.1016/j.actamat.2009.01.035.

[32] C. Puncreobutr, P.D. Lee, M. Kaye, D. Balint, D. Farrugia, T. Connolley, J. Lin, Quantifying damage accumulation during the hot deformation of free-cutting steels using ultra-fast synchrotron tomography, IOP Conf. Ser. Mater. Sci. Eng. 33 (2012). https://doi.org/10.1088/1757-899X/33/1/012038.

[33] T.P. Chapman, K.M. Kareh, M. Knop, T. Connolley, P.D. Lee, M.A. Azeem, D. Rugg, T.C. Lindley, D. Dye, Characterisation of short fatigue cracks in titanium alloy IMI 834 using X-ray microtomography, Acta Mater. 99 (2015) 49–62. https://doi.org/10.1016/j.actamat.2015.07.069.

[34] K.M. Kareh, P.D. Lee, R.C. Atwood, T. Connolley, C.M. Gourlay, Revealing the micromechanisms behind semi-solid metal deformation with time-resolved X-ray tomography, Nat. Commun. 5 (2014) 1–7. https://doi.org/10.1038/ncomms5464.

[35] M.A. Azeem, M.K. Bjerre, R.C. Atwood, N. Tiedje, P.D. Lee, Synchrotron quantification of graphite nodule evolution during the solidification of cast iron, Acta Mater. 155 (2018) 393–401. https://doi.org/10.1016/j.actamat.2018.06.007.

[36] N.S. Tiedje, M.K. Bjerre, M.A. Azeem, J.H. Hattel, P.D. Lee, Analysis of Local Conditions on Graphite Growth and Shape During Solidification of Ductile Cast Iron, Trans. Indian Inst. Met.

71 (2018) 2699–2705. https://doi.org/10.1007/s12666-018-1448-z.

[37] M.K. Bjerre, M.A. Azeem, N.S. Tiedje, J. Thorborg, P.D. Lee, J.H. Hattel, A graphite nodule growth model validated by in situ synchrotron x-ray tomography, Model. Simul. Mater. Sci. Eng. 26 (2018). https://doi.org/10.1088/1361-651X/aae9ce.

[38] R.C. Atwood, S. Sridhar, W. Zhang, P.D. Lee, Diffusion-controlled growth of hydrogen pores in aluminium-silicon castings: In situ observation and modelling, Acta Mater. 48 (2000) 405–417. https://doi.org/10.1016/S1359-6454(99)00363-8.

[39] J. Eiken, E. Subasic, J. Lacaze, 3D phase-field computations of microsegregation in nodular cast iron compared to experimental data and Calphad-based Scheil-prediction, Materialia. 9 (2020) 100538. https://doi.org/10.1016/j.mtla.2019.100538.

[40] M. Drakopoulos, T. Connolley, C. Reinhard, R. Atwood, O. Magdysyuk, N. Vo, M. Hart, L. Connor, B. Humphreys, G. Howell, S. Davies, T. Hill, G. Wilkin, U. Pedersen, A. Foster, N. De Maio, M. Basham, F. Yuan, K. Wanelik, I12: The Joint Engineering, Environment and Processing (JEEP) beamline at Diamond Light Source, J. Synchrotron Radiat. 22 (2015) 828–838. https://doi.org/10.1107/S1600577515003513.

[41] N. Wadeson, M. Basham, Savu: A Python-based, MPI Framework for Simultaneous Processing of Multiple, N-dimensional, Large Tomography Datasets, ArXiv. abs/1610.0 (2016). http://arxiv.org/abs/1610.08015%0Ainternal-pdf://0.0.0.96/1610.html.

[42] N.T. Vo, R.C. Atwood, M. Drakopoulos, Superior techniques for eliminating ring artifacts in X-ray micro-tomography, Opt. Express. 26 (2018) 28396. https://doi.org/10.1364/oe.26.028396.

[43] G.A. Holzapfel, Nonlinear Solid Mechanics: A Continuum Approach, John Wiley & Sons Ltd., 2000. https://books.google.co.uk/books/about/Nonlinear_Solid_Mechanics.html?id=_ZkeAQAAIAAJ&source=kp_cover&redir_esc=y.

[44] J. Qing, V.L. Richards, D.C. Van Aken, Examination of Nodular Graphite Formation and Austenite Solidification in Ductile Iron, Trans. Am. Foundry Soc. (2015) 271–281.

[45] R. Ghergu, L. Magnusson Åberg, J. Lacaze, A possible mechanism for the formation of exploded graphite in nodular cast irons, Mater. Sci. Forum. 790–791 (2014) 435–440. https://doi.org/10.4028/www.scientific.net/MSF.790-791.435.

[46] F. Rapatz, H. Pollack, Ueber Schwarzbruch (Black fracture), Stahl Und Eisen. 44 (1924) 1509–1514.

[47] C. Loper, R. Heine, Dendritic structure and spiking in ductile iron, AFS Trans. 76 (1968) 547–554.

[48] M. Gagne, R. Goller, Plate Fracture in Ductile Iron Castings, Ions Am. Foundrymen's Soc. 91 (1983) 37–46.